JOURNAL OF PROPULSION AND POWER
Vol. 12, No. 3, May–June 1996

Simplified Model and Navier–Stokes Calculations for Hypersonic Air Intakes Design

O. Penanhoat*
SNECMA, 77550 Moissy Cramayel, France
and
D. Darracq†
ONERA, 92322 Chatillon, France

Air intakes constitute a major component in scramjet propulsion systems. To design them properly, efficient and accurate numerical methods are necessary. Devoted to a particular family of air intakes, we present a simplified model that cannot simulate the complete structure of the flow and complex phenomena such as separation, but ensures high efficiency. More physical accuracy is obtained due to a Navier–Stokes code where the saving of computational time is achieved with a lower, upper k-ε implicit algorithm. The simplified model and the Navier–Stokes code are applied to a recent experimental configuration tested at Mach 5; analyses of the numerical predictions and of the experimental results are carried out. Both of the simulations for design are discussed.

I. Introduction

WITHIN the frame of studies devoted to hypersonic air intakes design, we are interested in both efficient and physically accurate numerical predictions of their performances. Accuracy is achieved in Navier–Stokes codes that have been largely developed, and new studies improve either the physical models or the convergence rate. However, concerning design, these calculations remain expensive if we wish to evaluate a high number of geometries and select the best one. More particularly, when an optimization algorithm is to be used for an air intake defined by a set of various parameters (minimizing an objective function as in Ref. 1), a great number of calculations are required and this excludes the use of Navier–Stokes calculations. There is therefore a specific need for a very efficient calculation technique with an eventual reduced accuracy. We present a simplified model that cannot take into account complex phenomena occurring in the flow such as separation, but ensures a high efficiency. Navier–Stokes calculations remain useful at the terminal stage of the design where a more realistic estimation of performances helps to correct obvious imperfections of the geometry. We used a k-ε turbulent Navier–Stokes code FLU3M developed mainly at ONERA. An implicit treatment of lower (L), upper (U) type could increase convergence rate.

First we briefly describe a particular mixed compression hypersonic air intakes family that we considered for this study. We also present a test case defined at SNECMA, which was experimented at Mach 5 at ONERA, and upon which we performed our numerical predictions for comparison. Next, we describe the simplified model calculation technique and give the results obtained on the previous test case. Lastly, the main features of the Navier–Stokes code that was employed are given and we focus on the implicit LU technique. Results on the test case are analyzed and compared with simplified model calculations and experimental results.

Received March 6, 1995; presented as Paper 95-6016 at the AIAA/AAAF/DGLR/JSASS/RAeS 6th International Aerospace Plane and Hypersonics Technologies Conference, Chattanooga, TN, April 3–7, 1995; revision received Sept. 1, 1995; accepted for publication Sept. 12, 1995.

*Dr. Ing., Villaroche Center.
†Dr. Ing., Aerodynamic Division, BP 72.

II. Mixed Compression Air Intakes and Test Case

There are various types of hypersonic air intakes whose designs may be quite different. We have chosen a particular family of mixed compression air intakes as illustrated in Fig. 1. The compression scheme is the same as given in Ref. 1 and some similar features may be found in other references.[2–4] A two-dimensional compression is realized up to the chamber entrance. It is composed of an external compression on a polyhedric ramp, followed by an internal compression in a diffuser. The external geometry is designed so that the generated oblique shocks do not go into the diffusor on the whole air intake entrance Mach number M_0 range. They focus on the cowl lip at a M_0 value, which we call the external adaptation Mach number, and we consider this value as the upper limit of the M_0 range. The internal cowl edge is polyhedric, and the internal part of the ramp is still polyhedric, but it is constructed so that no reflection of cowl shocks appears for a particular value of M_0, which we call the internal adaptation Mach number. The entrance station (foot of the external ramp) and exit station (chamber entrance) will be designated, respectively, as stations 0 and 2. At station 0, for a given M_0, airflow is captured on the height H_0. Exit section has a constant height H_2.

In practical cases, lateral spillage effects on the external ramp or viscous effects on the side wall would appear and make the flow three dimensional, but we consider here that the air intake is wide enough for these effects to be negligible.

We see that the external two-dimensional compression is achieved due to outward turning of the flow, whereas internal two-dimensional compression is obtained by inward turning of the flow. We do not, however, impose a total turning equal to zero. The optimum amount of turning should be evaluated by

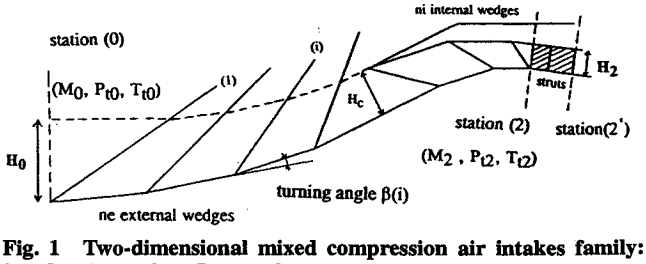

Fig. 1 Two-dimensional mixed compression air intakes family: M = Mach number, P_t = total pressure, and T_t = total temperature.

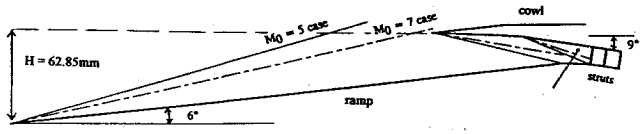

Fig. 2 Geometry of the tested air intake: M_2 = 3.4 for M_0 = 5 (γ = 1.35) and M_2 = 4.5 for M_0 = 7 (γ = 1.35).

taking into account the whole propulsive system. Moreover, the intake allows a uniform flow at the exit station for one value of M_0 (which is the internal adaptation Mach number), and therefore avoids big heterogeneities at the chamber entrance. This property may be an advantage for the chamber design.

Up to this point we supposed implicitly that no viscous effect was present in the compression scheme defining this family. Practically, it is not the case, but we expect that viscous effects of the real flow will not change the compression scheme dramatically. In particular, it means that the interaction of oblique shocks with the boundary layer will be weak enough to prevent separation. This hypothesis is made in the following simplified model calculations and will consequently be validated by a full Navier–Stokes calculation.

We now present the experimental test case selected for comparison with numerical predictions. The air intake geometry given in Fig. 2 has only a single turning angle external compression ramp fixed at 6 deg to prevent the risk of separation. The cowl has two turning angles (2.41 and 8.69 deg, respectively) and is constructed so that internal adaptation with inviscid hypothesis is satisfied for M_0 = 5 for a calorically perfect gas with γ = 1.35 (γ being the specific heats ratio). In the experiment, a row of vertical struts was located at the end of the air intake, their leading edge being just after the last slope discontinuity of the ramp wall. This station is what we considered as the air intake exit in this article. Its height H_2 is equal to 12.1 mm. For M_0 = 5, H_0 = 50 mm, and the uniform flow obtained at the exit station, M_2 = 3.4. With γ = 1.35, external adaptation is obtained for M_0 = 7.51. The intake produces an inward total turning of the flow equal to 9 deg.

Experiments were performed with air; calorically perfect gas hypothesis was satisfied with γ = 1.4. At the air intake entrance, the total pressure of the flow for M_0 = 5 was p_{t0} = 34*b* and the total temperature was T_{t0} = 544 K. A flat plate in front of the intake simulated a forebody. It generated a boundary-layer displacement thickness of δ_{10} = 2.5 mm. Many static pressure probes were located along the ramp and cowl walls. The exit station was swept with a static and pitot pressures probe rake. More complete information on this experiment may be found in Ref. 5 (M_0 = 7 was also tested).

III. Simplified Model Calculation Technique

The simplified calculation of an air intake belonging to the previous family is made in three steps: 1) a coupled boundary-layer oblique shocks calculation on the polyhedric profile of the external ramp, 2) a calculation of the same type on the polyhedric profile of the internal cowl edge using the flowfield obtained at the end of the external ramp, and 3) a particular treatment on the internal ramp side. Then an average that we call conservative is made in the exit section.

Also, the flow encountered for such air intakes is generally turbulent and this assumption is retained in the simplified calculations.

A. Coupled Boundary-Layer Oblique Shocks Calculations on a Polyhedric Profile

We consider a polyhedric profile formed with n straight segments turning consecutively with an angle β_i (i = 1, n) and the angle β_1 is the turning of the first segment from an initial straight wall. This profile and the upstream plane wall define

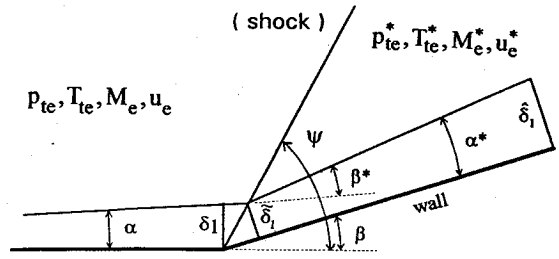

Fig. 3 Boundary-layer oblique shock-coupled calculation on a wedge.

n wedges that we designed by their angles β_i. At the origin of the profile (upstream extremity of the first segment) the flowfield is given and defined by a uniform state outside of the boundary layer and by the specification of the displacement thickness δ_1, the momentum thickness θ, and energy thickness Δ of the boundary layer at this station (noted, respectively, δ_{10}, θ_0, and Δ_0). Furthermore, if δ_{10} is not equal to zero, we give the angle $\arctan(d\delta_1/dx)$, where x is the direction of the plane wall in front of the polyhedric ramp. The calculations of the variations of θ and Δ along the profile do not participate in the coupling and may be performed after. The whole calculation on the polyhedric profile is decomposed in n successive coupled calculations on each wedge β_i (i = 1, n) and the associated downstream segment.

If the flowfield in front of the oblique shock produced by the wedge β_i is given or previously calculated, an iterative procedure is used to calculate the flowfield at the end of the downstream segment. This iterative procedure is based on the classical direct coupling technique with alternatively a Euler calculation on the wall thickened with the displacement thickness (called external solution) and a boundary-layer calculation with the new external solution. Nevertheless, simplifying approximations have been introduced and are mainly as follows.

1) If the displacement thickness δ_1 just before the upstream extremity of the considered wall segment is given, a jump relation of δ_1 through the oblique shock is used, which conserves the mass (see notations in Fig. 3):

$$\frac{\tilde{\delta}_1}{\sin(\psi - \beta)} = \frac{\delta_1}{\sin(\psi)} \tag{1}$$

where ψ is the angle of the oblique shock with the first straight segment of the wedge.

2) Another approximation is the evolution of the displacement thickness on the segment after the oblique shock is calculated due to a flat plate approximation with compressibility effects for a turbulent flow and an adiabatic wall.[6] We must first research a fictitious leading-edge point such that a flat plate approximation of the boundary-layer development would produce $\tilde{\delta}_1$ for the external flow given by (p^*_{te}, T^*_{te}, M^*_e), which are, respectively, the external total pressure, total temperature, and Mach number. Then we derive $\hat{\delta}_1$ at the end of the segment.

3) The flow being turbulent, the evolution of δ_1 is expressed as d^λ, where d is the distance from the fictitious leading-edge point and $\lambda = \frac{5}{6}$. We assume that δ_1 varies linearly between $\tilde{\delta}_1$ and $\hat{\delta}_1$. This hypothesis would be less justified in a laminar regime where $\lambda = \frac{1}{2}$. As a result, the thickened wall profile is still a wedge whose angle is $\beta^* = \beta + \alpha^* - \alpha$. This permits the use of a simple oblique shock calculation to evaluate the new external solution.

4) The oblique shock calculation is realized either with a calorically perfect gas hypothesis (retained here for the test case) or an equilibrium gas hypothesis.

After the iterative calculation on the polyhedric profile has been performed, θ and Δ evolutions are estimated by the following approximate procedure:

5) Firstly, jump equations for θ and Δ are applied through each oblique shock. We satisfy a conservation principle, respectively, for the momentum and the energy, through the shock line. Regarding the momentum conservation, we choose either the conservation of the momentum component, which is parallel to the shock line [Eq. (2a)] or the component that is perpendicular to it [Eq. (2b)]. Noting u_e the external velocity, jump formulas are

$$\frac{\tilde{\theta}}{\sin(\psi - \beta)} = \frac{\theta}{\sin(\psi)} \tag{2a}$$

$$u_e^* \times (\tilde{\theta} + \tilde{\delta}_1) = u_e \times (\theta + \delta_1) \tag{2b}$$

$$\frac{\tilde{\Delta}}{\sin(\psi - \beta)} = \frac{\Delta}{\sin(\psi)} \tag{2c}$$

The simplified model cannot satisfy the conservation of the two components of the momentum [Eq. (2a) or (2b) is sufficient for the determination of $\tilde{\theta}$]. It is preferable in the case of oblique shocks to conserve the parallel component that is predominant. That is what we did here.

6) Secondly, the evaluations of θ and Δ on the wedge after the oblique shock are done with a flat plate approximation, in the same way as for δ_1.

Concerning the calculation on the polyhedric profile of the internal cowl edge, we take the external solution at the end of the external compression ramp for upstream conditions, and an initial boundary-layer thickness equal to zero (leading edge of the cowl). It should be pointed out that, due to the boundary-layer growth on the external ramp, the incidence of the flow on the internal cowl edge is stronger.

B. Treatment on the Ramp Inside the Diffusor

The calculation of the flow inside the diffusor, on the ramp side, is less accurate than on the internal cowl edge side. This is due to the following stronger approximations:

First we suppose that we are close to the internal adaptation; this means that the exact Navier–Stokes solution would have oblique shocks generated by the cowl edge that would impact the internal ramp in the neighborhood of wall slope discontinuities and would therefore have nearly no reflection. Then, we neglect the boundary-layer growth on each segment of the internal ramp.

This leads us to apply only jump relations on δ_1, θ, and Δ through each oblique shock impacting the internal ramp. These relations are similar to those already given [see Eqs. (1) and (2a–2c)], knowing that in this case $\beta < 0$ and $\psi > \pi/2$.

C. Flow Rates and Conservative Averages in the Exit Section

Let p_2, ρ_{e2}, u_{e2}, and h_{te2} be, respectively, the pressure, the external mass per volume unit, the external velocity, and the external total enthalpy taken in the exit station 2 and derived by the calculation on the polyhedric profile of the internal cowl edge. The values of δ_1, θ, and Δ obtained in station 2 on the cowl edge are noted (δ_{12}^c, θ_2^c, and Δ_2^c) and (δ_{12}^r, θ_2^r, and Δ_2^r) on the ramp side. Carrying out the classical corrections on flow rates due to the boundary layer and introducing the corrected mass flow in the expressions of the corrected flow rates of momentum and energy, we obtain:

$$Q_{m2} = \rho_{e2}u_{e2}(H_2 - \delta_{12}^c - \delta_{12}^r) \tag{3a}$$

$$Q_{i2} = p_2H_2 + u_{e2}Q_{m2} - \rho_{e2}u_{e2}^2(\theta_2^c + \theta_2^r) \tag{3b}$$

$$Q_{e2} = Q_{m2}h_{te2} + \rho_{e2}u_{e2}h_{te2}(\Delta_2^c + \Delta_2^r) \tag{3c}$$

We do not apply formulas (3a) and (3c) because the calculation of δ_{12}^r is principally approximated and a consequence is that we would not ensure conservation principle. We take advantage of the fact that the exact Navier–Stokes solution (which we wanted to approach), conserves rigorously the mass flow and the energy flow between the section of flow capture and the exit station. After having calculated H_0, we express Q_{m2} and Q_{e2} by

$$\begin{aligned} Q_{m2} &= Q_{m0} = \rho_{e0}u_{e0}(H_0 - \delta_{10}) \\ Q_{e2} &= Q_{e0} = Q_{m0}h_{te0} + \rho_{e0}u_{e0}h_{te0}\Delta_0 \end{aligned} \tag{4}$$

where index 0 designates the station 0.

Once the flow rates have been calculated, we evaluate an equivalent average state in the exit station. We retain an average that we qualify conservative, derived by searching the uniform state that would produce the same flow rates of mass, momentum, and energy. For a calorically perfect gas with γ = constant, the conservative averaged velocity $\bar{u}_2$ is the solution of a simple second-order polynomial equation where the unknown is noted v:

$$\frac{\gamma + 1}{2(\gamma - 1)} Q_{m2}v^2 - \frac{\gamma}{(\gamma - 1)} Q_{i2}v + Q_{e2} = 0 \tag{5}$$

For an equilibrium gas, an iterative procedure is used.

D. Application to the Experimental Test Configuration

This procedure was applied to the test case described previously with $M_0 = 5$ and $\delta_{10} = 2.5$ mm. The value of θ_0 was estimated from δ_{10} with a flat plate approximation. The value Δ_0 estimated in the same way remained negligible compared to δ_{10}. The initial growth α_0 of the boundary layer was taken equal to zero. Figure 4 shows the oblique shocks obtained, the captured flow tube, and the dashed lines show the profile of the wall thickened by the boundary-layer displacement thickness. On the internal cowl side, this profile is very close to the wall because the boundary layer is hardly developed. Figure 5 gives the external Mach number distribution (outside of the boundary layer) on the ramp and the cowl sides. The evolutions of δ_1 and θ along the ramp and the cowl are also given; δ_1 decreases through the first oblique shock, increases along the external ramp segment, and decreases strongly inside the diffusor. At station 2, $\delta_{12}^r/H_2 = 0.079$ and $\delta_{12}^c/H_2 = 0.026$. Energy thickness varies slightly only through shocks and remains small. The conservative average in station 2 leads to the values given in the second line of Table 1. The ratio of the conservative averaged total pressure $\bar{p}_{i2}$ on the external total pressure p_{te0} at station 0, gives the mean efficiency $\bar{\eta}_{02} = 0.52$.

IV. Navier–Stokes Simulations

The Navier–Stokes simulations were performed with the FLU3M code,[7] which solves the Euler or Navier–Stokes equa-

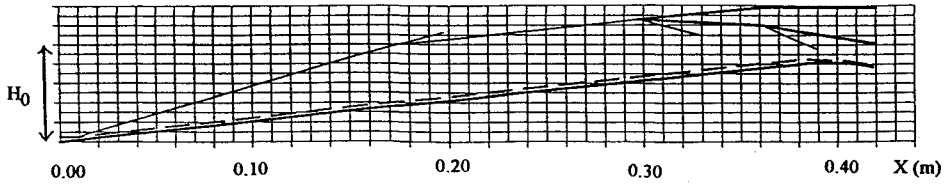

Fig. 4 Simplified model calculation at Mach 5.

Table 1 Comparison of global performance predictions

Prediction	M_{2max}	η_{02max}	$\bar{M}_2$	$\bar{\eta}_{02}$
Experiments	3.50	0.90	2.45	0.40
Simplified model	3.25	0.88	2.75	0.52
FLU3M k-ε code	3.26	0.88	2.83	0.52

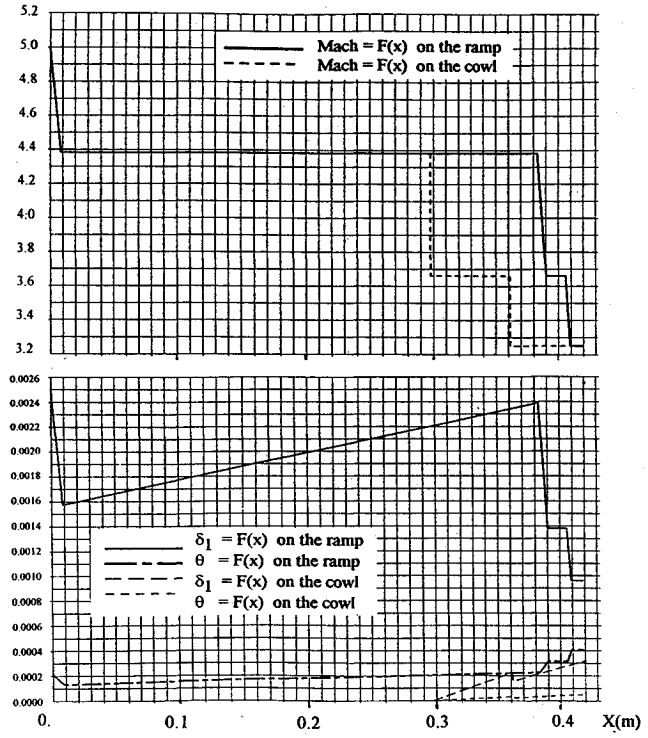

Fig. 5 External Mach, δ_1, and θ distributions on the ramp and cowl.

tions in a finite volume formulation on block-structured grids. Convective terms are discretized with Roe's upwind solver (with vanishing entropy fix near the walls, as in Ref. 8), associated with monotonic upwind schemes for conservation laws (MUSCL) interpolation. Viscous fluxes are discretized with a standard centered scheme. The k-ε two-equation turbulence model has been implemented in the code by Charmant and Cambier.[9] The Launder–Sharma model,[10] which results from an optimization of the Jones–Launder model,[11] is used in this work. A turbulent length scale correction proposed by Vuong and Coakley[12] is added to this model to take into account compressibility effects that may be not negligible at Mach 5. An investigation of compressibility models has been presented in Ref. 13 on a compression corner (34, 36, and 38 deg) at Mach number 9.22. It has been concluded that the model was efficient for predicting accurately separation length, pressure, and surface heat fluxes.

Initially, an alternating direction implicit (ADI) factorization was used to solve the implicit operator. To increase robustness and efficiency, an LU factorization extended to k-ε models has been developed. It is shown that this scheme permits the use of very high Courant–Friedrichs–Lewy (CFL) numbers and to highly reduced CPU time.

A. Implicit Algorithm

We preferred as a LU algorithm a diagonal dominant one ($DDLU$) and a new extension was made to the k-ε equations.

We consider the convective part of the turbulent Navier–Stokes equations introducing the conservative vector $\boldsymbol{Q}$ and the flux vectors $\boldsymbol{E}$ and $\boldsymbol{F}$ in the two directions ξ and η:

$$\boldsymbol{Q}^{n+1} - \boldsymbol{Q}^n + \Delta t(\partial_\xi \boldsymbol{E}^{n+1} + \partial_\eta \boldsymbol{F}^{n+1}) = 0 \tag{6}$$

The flux vectors are nonlinear functions of Q. Linearizing, we obtain

$$\begin{aligned} \boldsymbol{E}^{n+1} &= \boldsymbol{E}^n + \boldsymbol{A}^n\Delta\boldsymbol{Q}^n + \mathbb{O}(\Delta t^2) \\ \boldsymbol{F}^{n+1} &= \boldsymbol{F}^n + \boldsymbol{B}^n\Delta\boldsymbol{Q}^n + \mathbb{O}(\Delta t^2) \end{aligned} \tag{7}$$

where $\Delta\boldsymbol{Q}^{n+1} = \boldsymbol{Q}^{n+1} - \boldsymbol{Q}^n$ and $\boldsymbol{A}$ and $\boldsymbol{B}$ are the flux Jacobians $\partial\boldsymbol{E}/\partial\boldsymbol{Q}$ and $\partial\boldsymbol{F}/\partial\boldsymbol{Q}$. These Jacobian matrices include the convective part of the k-ε equations. Applying Eq. (6) to Eqs. (7) produces the delta form of the algorithm, where $\boldsymbol{R}$ is the residual:

$$(\boldsymbol{I} + \Delta t\partial_\xi \boldsymbol{A}^n + \Delta t\partial_\eta \boldsymbol{B}^n)\Delta\boldsymbol{Q} = -\Delta t\boldsymbol{R} \tag{8}$$

Jameson and Turkel[14] constructed a scheme involving $\boldsymbol{L}$ and $\boldsymbol{U}$ triangular matrices:

$$\boldsymbol{LU}.\Delta\boldsymbol{Q} = -\Delta t\boldsymbol{R} \tag{9a}$$

$$\begin{aligned} \boldsymbol{L} &= [\boldsymbol{I} + \Delta t(\partial_\xi^- \boldsymbol{A}^+ + \partial_\eta^- \boldsymbol{B}^+)] \\ \boldsymbol{U} &= [\boldsymbol{I} + \Delta t(\partial_\xi^+ \boldsymbol{A}^- + \partial_\eta^+ \boldsymbol{B}^-)] \end{aligned} \tag{9b}$$

To increase the robustness, Yoon and Jameson[15] proposed a diagonal form that may be called $DDLU$ (by reference to $DDADI$):

$$\boldsymbol{LD}^{-1}\boldsymbol{U}.\Delta\boldsymbol{Q} \quad -\Delta t\boldsymbol{R} \tag{10a}$$

$$\begin{aligned} \boldsymbol{L} &= [\boldsymbol{I} + \Delta t(\partial_\xi^- \boldsymbol{A}^+ + \partial_\eta^- \boldsymbol{B}^+ - \boldsymbol{A}^- - \boldsymbol{B}^-)] \\ \boldsymbol{D} &= [\boldsymbol{I} + \Delta t(\boldsymbol{A}^+ + \boldsymbol{B}^+ - \boldsymbol{A}^- - \boldsymbol{B}^-)] \end{aligned} \tag{10b}$$

$$\boldsymbol{U} = [\boldsymbol{I} + \Delta t(\partial_\xi^+ \boldsymbol{A}^- + \partial_\eta^+ \boldsymbol{B}^- + \boldsymbol{A}^+ + \boldsymbol{B}^+)]$$

Among the many ways of splitting the Jacobian matrices, the Jameson and Turkel method augments diagonal dominance:

$$\boldsymbol{A}^+ = \tfrac{1}{2}[\boldsymbol{A} + \chi(\boldsymbol{A})\boldsymbol{I}], \qquad \boldsymbol{A}^- = \tfrac{1}{2}[\boldsymbol{A} - \chi(\boldsymbol{A})\boldsymbol{I}]$$

$$\text{with} \quad \chi(\boldsymbol{A}) = \beta \max(|\lambda_\xi|) \qquad \beta \geq 1 \tag{11}$$

λ_ξ are the eigenvalues of $\boldsymbol{A}$. A great interest of factorization (10) and splitting (11) is that $\boldsymbol{D}$ is reduced to a scalar form:

$$\boldsymbol{D} = \{1 + \Delta t[\chi(\boldsymbol{A}) + \chi(\boldsymbol{B})]\}\boldsymbol{I} \tag{12}$$

Concerning the viscous fluxes, their true linearization is substituted by the spectral radius μ_M of the Jacobian matrix. The term $-\Delta t\mu_M(\partial_\xi^2 + \partial_\eta^2)$ is added to the left-hand side (LHS) of Eqs. (9), increasing the diagonal dominance and preserving the scalar structure of the diagonal.

The k-ε two-equation models introduce source terms in the system. To prevent instability only the negative part of the source terms is linearized. One of the advantages of the $DDLU$ scheme is that these implicit source terms may not be split in each factor, because they are included in the diagonal D present in both matrices.

By sweeping forward (lower operator) and backward (upper operator) in the diagonal direction ($i + j$ constant), the inversion of the two LU factors can be fully vectorized, avoiding the recursive procedure occurring in the tridiagonal system. Furthermore, during the forward and backward inversions, all variables needed from the off-diagonals are already updated and can be moved to the right-hand side (RHS). Then only scalar diagonal terms remain on the LHS and there is no block matrix to invert.

This LU implicit solver is much more robust and faster than the ADI one. Tests on a turbulent flat plane indicate that the stability of this scheme is ensured for CFL as high as 10^8. The CPU times per point and per iteration for the code on a Cray

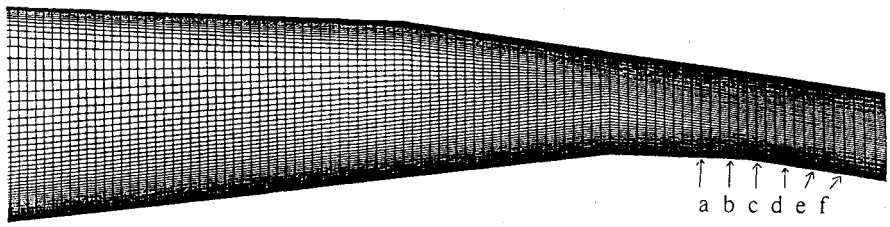

Fig. 6 Mesh points inside the diffusor (c = exit station 2).

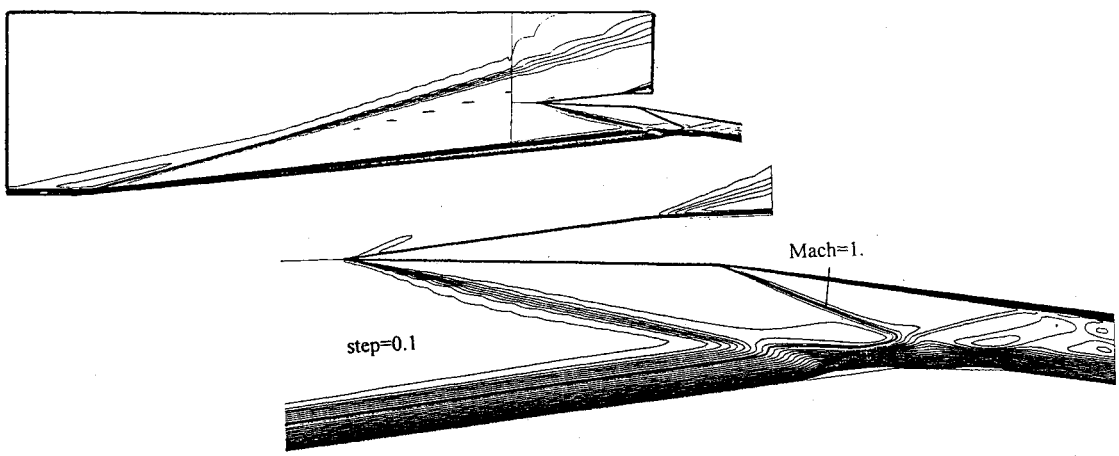

Fig. 7 Iso-Mach lines (*LU k-ε* FLU3M code).

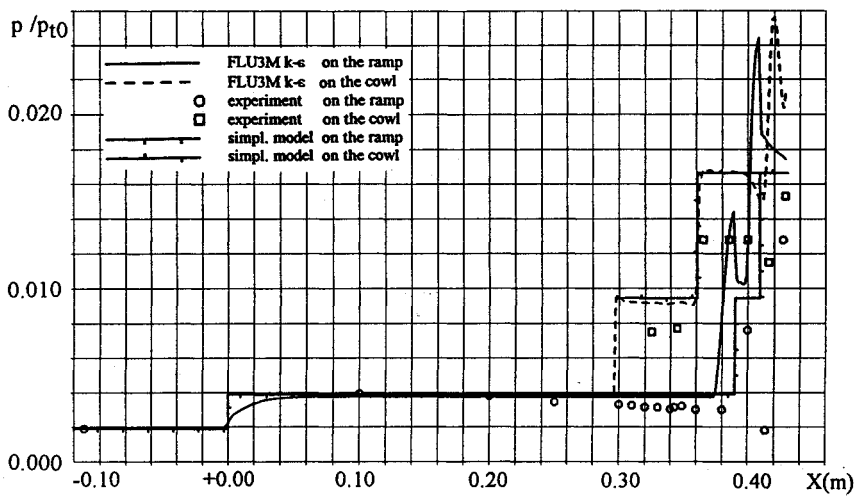

Fig. 8 Pressure distributions on the ramp and cowl.

Y-MP are 116 μs for ADI k-ε, 69 μs for ADI laminar, and 60 μs for *LU* k-ε schemes. This shows the interest of this last implicit scheme.

B. Application to the Experimental Test Configuration and Analysis

A three-block structured grid was realized on the experimental test configuration geometry, it contained (130 × 95), (120 × 117), and (75 × 95) points. Particular attention was paid to the refinement of the mesh inside the boundary layers. Preliminary evaluation of the simplified model was helpful in this task. About 50 points were distributed in the boundary-layer thickness, the first point being located at $y^+ \approx 1$ from the wall; the part of the mesh inside the diffusor is shown in Fig. 6.

Computation at Mach 5 was performed with the *LU* k-ε algorithm of the FLU3M code. Quality of the solution was partially evaluated by the calculation of the conservation of mass, momentum, and energy on each grid block. This was done by a balance between entering and exiting flow rates, and we achieved inside the diffusor block, which is the most critical, the following mass, x-momentum, y-momentum, and energy flow rates: 0.044, 0.75, 0.052, and 0.42. These values are quite satisfactory.

The main objective of this calculation was to predict precisely the structure of the flow in the diffusor and more particularly on the internal ramp. Iso-mach lines of Fig. 7 permit one to appreciate the flow qualitatively. Because of the initial value δ_{10} and its growth on the external ramp, a rather high boundary layer is observed at the diffusor entrance. Despite this, the flow upstream is only slightly disturbed on the opposite side of the duct. The two oblique shocks generated by the cowl are clean. Without any boundary layer on the ramp, they would hit the wall slightly before each of the two ramp points with slope discontinuity. What we observed above all was their interactions with the ramp boundary layer. Examin-

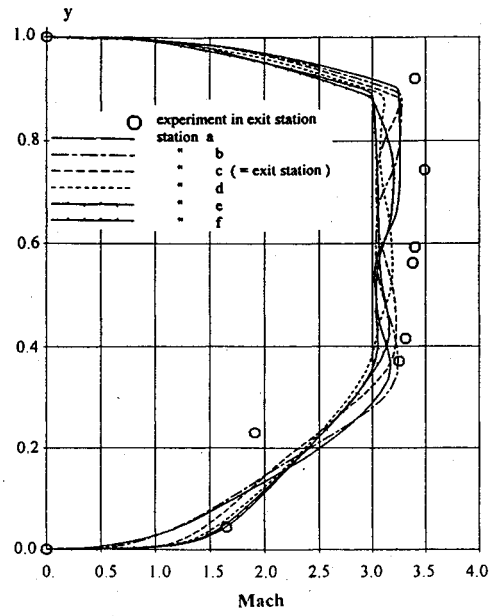

Fig. 9 Mach number profiles around air intake exit.

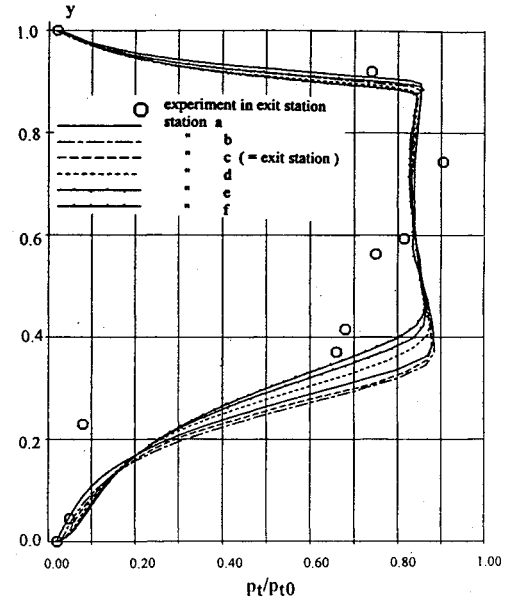

Fig. 10 Total pressure efficiency profiles around air intake exit.

ing the line Mach = 1 along the ramp wall, it seems that two small separation zones are developed. In fact, after an analysis of the velocity field, we find that only a small separation takes place at the interaction of the first oblique shock with the boundary layer. The accelerations due to the ramp slope discontinuities prevent important separations from appearing and disturbing all of the flow. Nevertheless, a small reflection of the second shock is produced.

Wall pressure distribution on the ramp and on the cowl given by FLU3M are compared with the experimental results and the simplified model predictions in Fig. 8. Comparing first with the simplified code, we observe the same levels on the external ramp and on the cowl edge, except at its end. However, the Navier–Stokes calculation shows two peaks on the ramp and one on the cowl. This can be explained by the interactions of the two oblique shocks with the boundary layer and by the impact of the weak oblique shock generated by the reflection of the second cowl oblique shock. We note that after the three peaks, the pressure level decreases nearly to that of the simplified model level. The comparison with experimental results is not very good. Some of the discrepancies may come from a rather high uncertainty of the experimental measurements. It also seems that experimental lateral spillage was not so negligible and resulted in a loss of pressure, especially on the cowl side. If this was the case, three-dimensional numerical simulations would be more representative.

Figures 9 and 10 show the Mach and total pressure distributions at the end of the diffusor, in a few stations whose positions are given in Fig. 6. Comparisons with the experiment are better here, although more experimental points would have been useful. These profiles reveal that in the vicinity of the exit, the flow does not change a lot longitudinally; above all, we see that the flow is rather uniform in about two-thirds H_2 on the cowl side and that the inevitable ramp boundary layer invades about one-third H_2 of the canal height.

Finally, we completed Table 1 with the results of the *LU* k-ε FLU3M code and of the experience where a conservative average was also performed. The simplified model and FLU3M results match very well. Comparisons with experiment are still not quite satisfactory, especially for averaged values. We justify this as previous discrepancies. We have noticed that by taking only the third experimental point (from $y = 0$) closer to numerical curves on Figs. 9 and 10, the averaged values become similar to numerical predictions.

V. Conclusions

To design hypersonic air intakes carefully we presented two types of simulations:

1) A simplified model whose advantage is efficiency; it is based on a boundary-layer oblique shock-coupled calculation with jump conditions through shock discontinuities.

2) Navier–Stokes calculations that can better predict complexity features such as separation; an implicit *LU* algorithm permitted us to save computational time and reach high CFL numbers.

Numerical predictions by these two means were obtained on a test configuration that was experimented at Mach 5 in a wind tunnel at ONERA. Comparisons of the simplified model and the Navier–Stokes calculations are satisfactory. In particular, the same levels of pressure on the cowl edge were predicted, although only the Navier–Stokes code can predict peaks of pressure due to shock boundary-layer interactions. Moreover, at the exit station, simplified model and Navier–Stokes calculations match very well for the conservative average.

Concerning the comparison of both numerical calculations with experience, it is rather mediocre and doesn't permit a positive conclusion. We think nevertheless that we achieved a good quality in Navier–Stokes computation as demonstrated by conservative balances, and attribute discrepancies to measurements uncertainty and also to a probable lateral spillage in the experiment that is ignored in the two-dimensional simulation.

In conclusion, the comparisons of the simplified model and the Navier–Stokes calculations validate the simplified model. It is very efficient and its use is appropriate in an optimization algorithm in the first step of a two-dimensional hypersonic air intake design. The second step would be applying Navier–Stokes calculations to predict with more fineness the structure of the flow inside the diffusor and change, if necessary, the internal ramp profile where complex shock boundary-layer interactions occur.

Acknowledgment

This study was realized through the French PREPHA program. The authors wish to thank the direction of SNECMA and the DGA for permission to publish this paper, and ONERA for its cooperation in this work.

References

[1]Penanhoat, O., and Rollin, G., "Hypersonic Air-Intakes Design and Numerical Optimization," *IAC'94* (Moscow, Russia), 1994.

[2]Baranovsky, S., Gilevich, I., Davidenko, D., Kanin, K., Sukov, A., and Tikhonov, A., "A Program of the Scramjet Design and Optimization," AIAA Paper 91-5073, Dec. 1991.

[3]Ikawa, H., "Rapid Methodology for Design and Performance Prediction of Integrated Supersonic Combustion Ramjet Engine," *Journal of Propulsion and Power*, Vol. 7, No. 3, 1991, pp. 437–444.

[4]Krajewski, E., "Leistungsanalyse von Staustrahlantrieben mit Überschallverbrennung," *DGLR Jahrbuch 1993-II*, 1993, pp. 559–568.

[5]Penanhoat, O., "PREPHA—Essai de l'entrée d'air Snecma à Mach 5 et 7," Tech. Note No. 173/DR/94, SNECMA, 1994.

[6]Cousteix, J., "Aérodynamique—Turbulence et Couches Limites," CEPADUES Editions, 1989.

[7]Guillen, P., and Dormieux, M., "Design of a 3D Multidomain Euler Code," International Seminar on Supercomputing, Boston, MA, 1989.

[8]Darracq, D., and Gazaix, M., "Computation of Viscous Shock/Shock Interaction with an Upwind LU Implicit Scheme," *Proceedings of the 19th International Symposium on Shock Waves*, Univ. de Provence, Marseille, France, 1993, pp. 383–388.

[9]Charmant, S., and Cambier, L., "Calculs d'Écoulements Compressibles Turbulents Autour d'Arrière-corps avec Tuyère," *30ième Colloque d'Aérodynamique Appliquée*, Ecole Centrale de Nantes, France, 1993 (Paper 19).

[10]Launder, B. E., and Sharma, B. I., "Application of the Energy Dissipation Model of Turbulence to Calculation of Flow near a Spinning Disc," *Letters in Heat and Mass Transfer*, Vol. 1, No. 2, 1974, pp. 131–138.

[11]Jones, W. P., and Launder, B. E., "The Prediction of Laminarization with a Two-Equation Model of Turbulence," *International Journal of Heat and Mass Transfer*, Vol. 15, No. 2, 1972, pp. 301–314.

[12]Vuong, S. T., and Coakley, T. J., "Modeling of Turbulence for Hypersonic Flows with and Without Separation," AIAA Paper 87-0286, Jan. 1981.

[13]Darracq, D., "Etude Numérique d'Écoulements d'Entrées d'Air de Véhicules Hypersoniques," Thèse de Doctorat de l'Univ. de Poitiers, France, 1995.

[14]Jameson, A., and Turkel, E., "Implicit Schemes and LU Decomposition," *Mathematics of Computation*, Vol. 37, No. 156, 1981, pp. 385–397.

[15]Yoon, S., and Jameson, A., "Lower-Upper Symmetric Gauss-Seidel Methods for the Euler and Navier–Stokes Equations," AIAA Paper 87-600, Jan. 1987.